Supporting Information

In Situ Architecting Amorphous Manganese Oxide/MXene Heterostructure Electrode with Fast Ion Transport and Structural Stability in Aqueous Zn-Mn Batteries

Yang Song[a], Wang Zhan[a], Zhihao Wu[a], Qizhi Chen[c], Xiaohua Chen[a], Zuohua Liu[a,b],

Jun Du[a], Changyuan Tao[a,b,*], Qian Zhang[a,*]

[a]School of Chemistry and Chemical Engineering, Chongqing University, Chongqing

400044, China

[b]State Key Laboratory of Coal Mine Disaster Dynamics and Control, Chongqing

University, Chongqing, 400044, China

[c]Guangxi Huiyuan Manganese Industry Co., Ltd. Laibin City, Guangxi, 546138,

China

*Corresponding Author E-mail: taocy@cqu.edu.cn (Changyuan Tao)

*Corresponding Author E-mail: qianz@cqu.edu.cn (Qian Zhang)

Supporting Figure Contents

S1 Synthesis and materials characterization

Fig. S1. The SEM image and elemental mapping images of a-MnO$_2$/Ti$_3$C$_2$F.

Fig. S2. XRD patterns of Ti$_3$AlC$_2$ and Ti$_3$C$_2$F.

Fig. S3. The lattice of (004), (108) and (110) facets of Ti$_3$C$_2$F.

Fig. S4. N$_2$ adsorption–desorption isotherm and pore size distribution of Ti$_3$C$_2$F, a-MnO$_2$/Ti$_3$C$_2$F and a-MnO$_2$.

Fig. S5. EPR spectra of a-MnO$_2$/Ti$_3$C$_2$F and a-MnO$_2$.

S2 Electrochemical performance and ion diffusion kinetics

Fig. S6. Rate performance of α-MnO$_2$ and Ti$_3$C$_2$F.

Fig. S7. Cycle performance at 0.3 A g^{-1} of α-MnO$_2$ and Ti$_3$C$_2$F.

Fig. S8. GCD curves at various cycles of a-MnO$_2$.

Fig. S9. (a) CV curves of a-MnO$_2$ cathode at various scan rates; (b,c) *log(i)* vs *log(v)* plot of a-MnO$_2$/Ti$_3$C$_2$F and a-MnO$_2$; (d) diffusion and capacitive contributions of the a-MnO$_2$ at 0.3 mV s^{-1}; (e) capacitive contribution of the a-MnO$_2$ at various scan rates.

S3 Ions insertion/extraction and reversible conversion mechanism

Fig. S10. (a) Digital photos of the Zn//a-MnO$_2$/Ti$_3$C$_2$F system and (b) a-MnO$_2$/Ti$_3$C$_2$F cathode at different potentials during charging and discharging.

Fig. S11. I-t curves of a-MnO$_2$/Ti$_3$C$_2$F and a-MnO$_2$ from 1.9 V to 1.25 V and then to 0.8 V discharges.

Fig. S12. XRD patterns of a-MnO$_2$ cathode at different potentials during charging and discharging.

Fig. S13. SEM-EDS element analysis of the (a) a-MnO$_2$ and (b) a-MnO$_2$/Ti$_3$C$_2$F electrodes at different charge-discharge states charged to 1.9 V and then charged to 1.25 V.

S4 Evaluation of electrode materials stabilities

Fig. S14. Photographs of a-MnO$_2$/Ti$_3$C$_2$F and a-MnO$_2$ cathodes after 500 cycles under a current density of 0.3 A g^{-1}.

Fig. S15. ICP analysis of dissolved Mn in electrolyte after various cycles for a-MnO$_2$/Ti$_3$C$_2$F and a-MnO$_2$ cathodes.

Fig. S16. Heat absorption curves of a-MnO$_2$ and a-MnO$_2$/Ti$_3$C$_2$F at different heating rates.

S5 Density functional theory calculations

Fig. S17. The calculation models of the (a-b) α-MnO$_2$, a-MnO$_2$ and MXene, as well as optimized (c-d) α-MnO$_2$/MXene and a-MnO$_2$/MXene structures.

Table S1. Rate performance of MnO$_2$ analogue materials reported in literatures.

Table S2. a-MnO$_2$/Ti$_3$C$_2$F's GITT corresponding data.

Table S3. a-MnO$_2$/Ti$_3$C$_2$F's GITT corresponding data.

Table S4. E_a and R^2 values calculation for the cathode material of a-MnO$_2$/Ti$_3$C$_2$F using three models under different α values.

Table S5. E_a and R^2 values calculation for the cathode material of a-MnO$_2$ using three models under different α values.
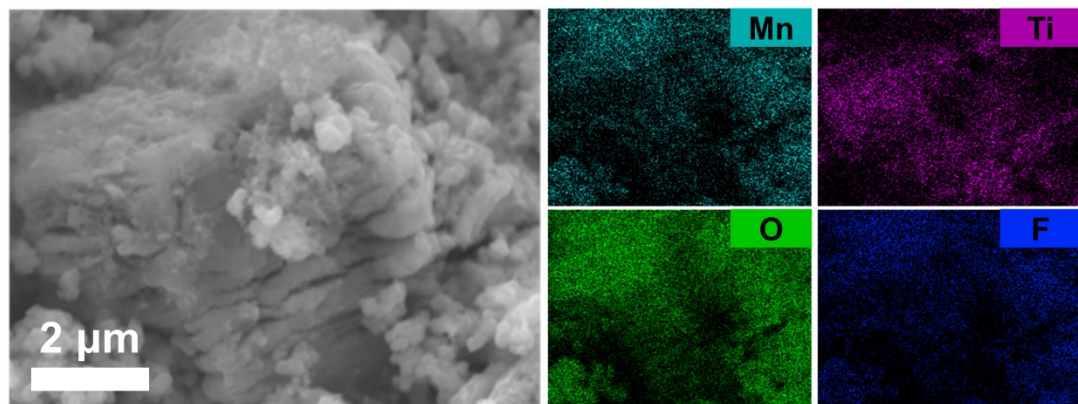
Figure S1. The SEM image and elemental mapping images of a-MnO$_2$/Ti$_3$C$_2$F.
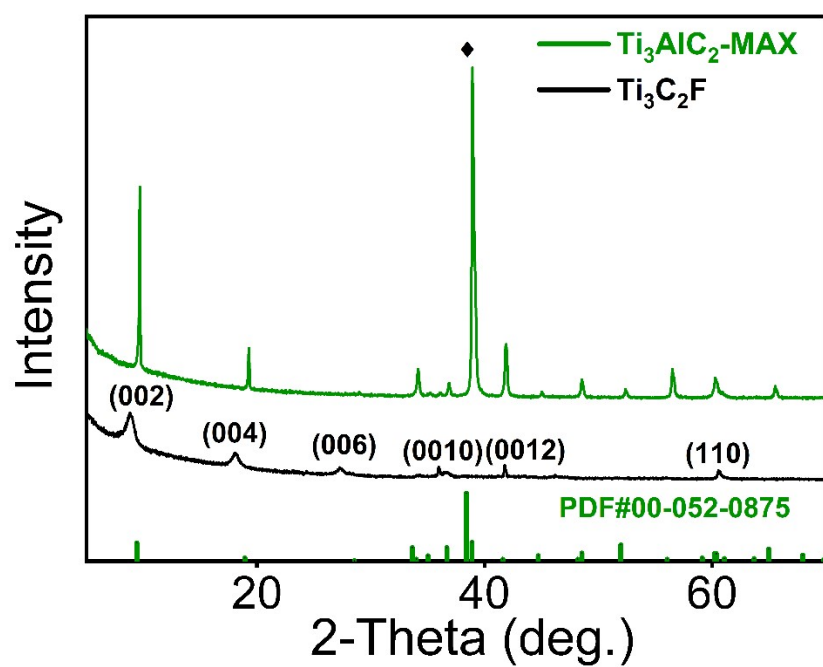

Figure S2. XRD patterns of Ti$_3$AlC$_2$ and Ti$_3$C$_2$F.
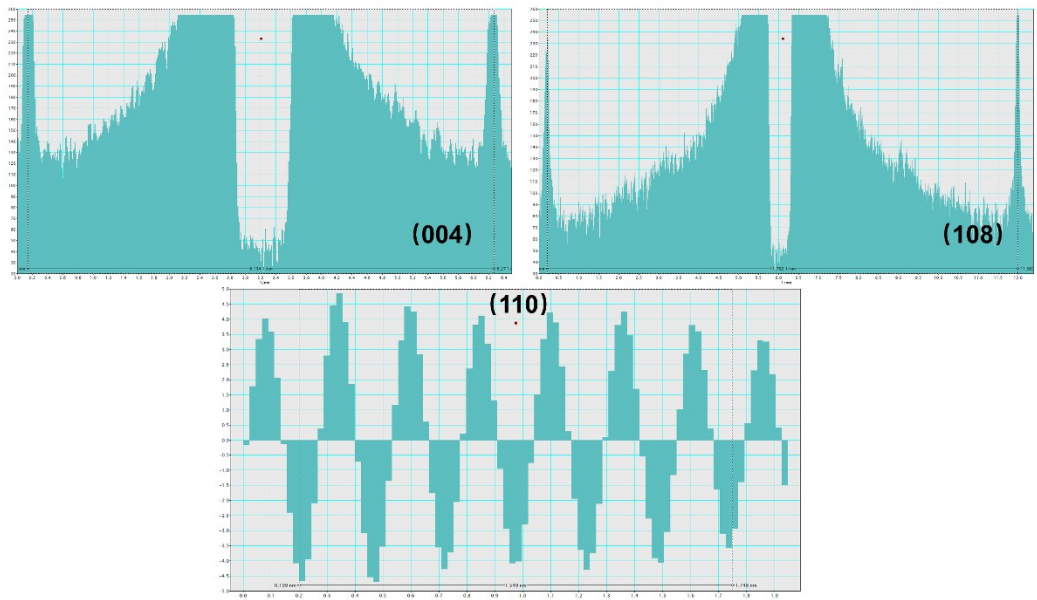
Figure S3. The lattice of (004), (108) and (110) facets of Ti$_3$C$_2$F.
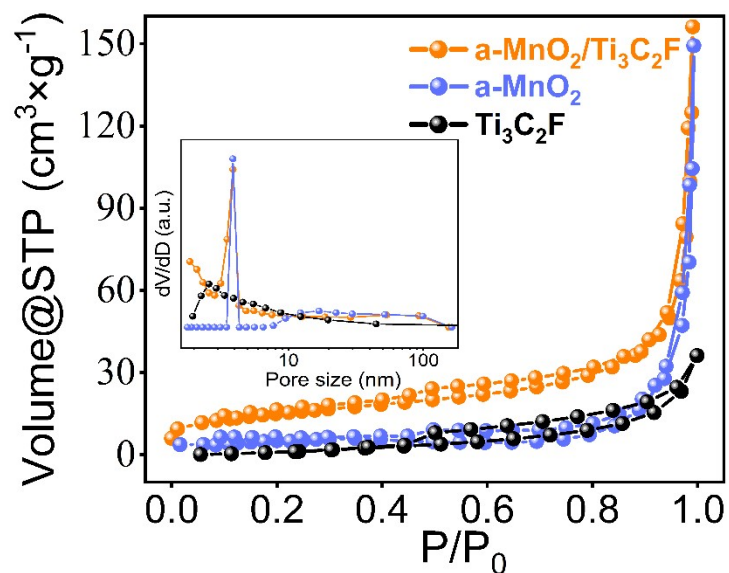
Figure S4. N$_2$ adsorption–desorption isotherm and pore size distribution of Ti$_3$C$_2$F, a-MnO$_2$/Ti$_3$C$_2$F and a-MnO$_2$.
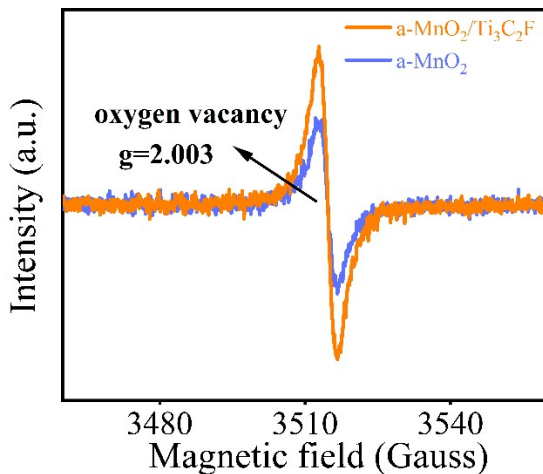
Figure S5. EPR spectra of a-MnO$_2$/Ti$_3$C$_2$F and a-MnO$_2$.

S2 Electrochemical performance and ion diffusion kinetics

α-MnO$_2$, has a tunnel structure of 2×2 and 1×1, which is an ideal positive electrode material due to its good structural stability and high theoretical capacity. Therefore, we established a corresponding battery comparison group to verify the superiority of a-MnO$_2$/Ti$_3$C$_2$F and Ti$_3$C$_2$F, as shown in Figure S6-7.
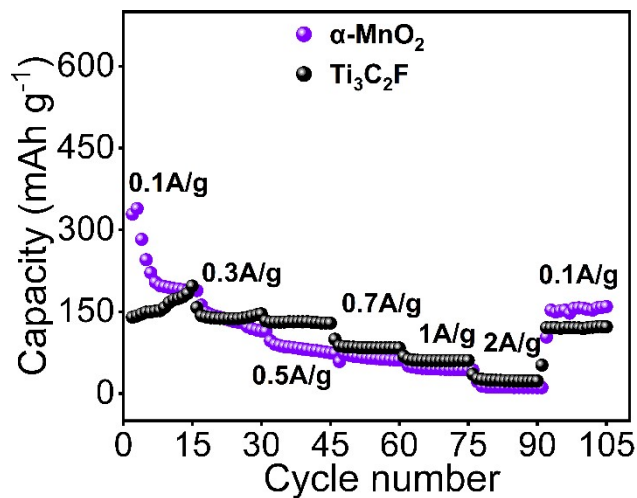
Figure S6. Rate performance of α-MnO$_2$ and Ti$_3$C$_2$F.
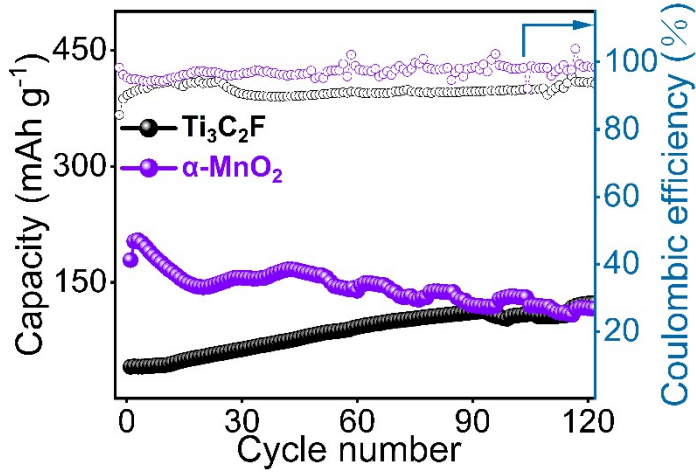
Figure S7. Cycle performance at 0.3 A g⁻¹ of α-MnO$_2$ and Ti$_3$C$_2$F.
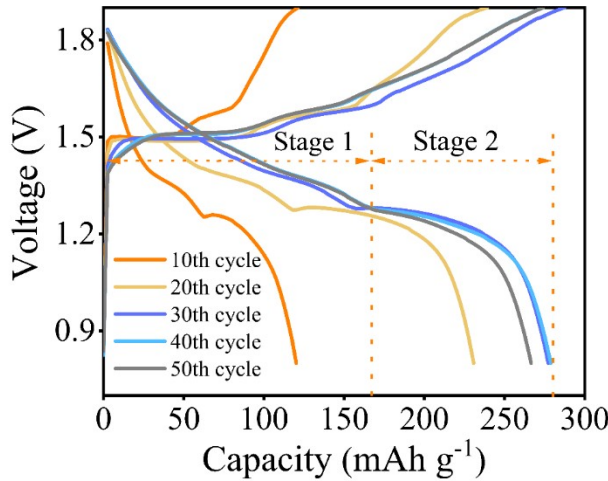
Figure S8. GCD curves at various cycles of a-MnO$_2$.

The charge-storage mechanism can be investigated by exploring the relationship between the peak current (*i*, mA) and the scan rates (*v*, mV s⁻¹) by Eq.(1)-(2):

$$i = av^b$$

$$\log (i) = b\log (v) + \log (a)$$

Where *a* and *b* are adjustable parameters. When *b* equals to 1, the capacity is fully governed by the capacitive-controlled process; if *b* equals to 0.5, it corresponds to a diffus ion-controlled process.[1, 2]

The respective contribution of capacitive-controlled processes and diffusion-controlled process can be quantitatively estimated through the following Eq.(3)-(4):

$$i(v) = k_1 v + k_2 v^{1/2}$$

$$i(v)/v^{1/2} = k_1 v^{1/2} + k_2$$

Where $i(v)$, $k_1 v$, $k_2 v^{1/2}$ and v refer to the current at a fixed potential, the capacitive-controlled current, the diffusion-controlled current and the scan rate, respectively.[3, 4]
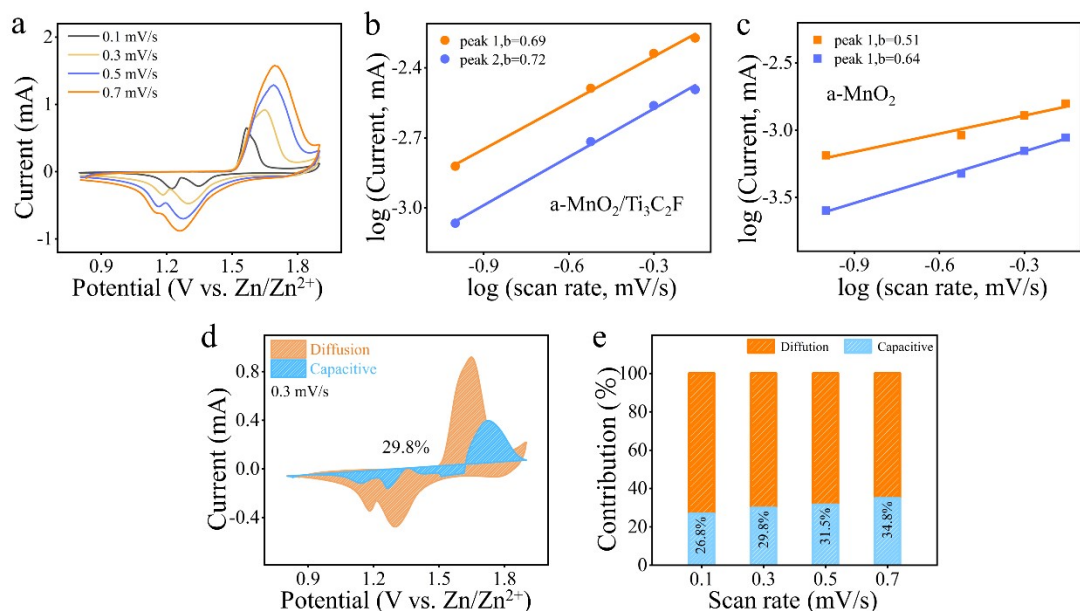
Figure S9. (a) CV curves of a-MnO$_2$ cathode at various scan rates; (b,c) log(i) vs log(v) plot of a-MnO$_2$/Ti$_3$C$_2$F and a-MnO$_2$; (d) diffusion and capacitive contributions of the a-MnO$_2$ at 0.3 mV s^{-1}; (e) capacitive contribution of the a-MnO$_2$ at various scan rates.

S3 Ions insertion/extraction and reversible conversion mechanism
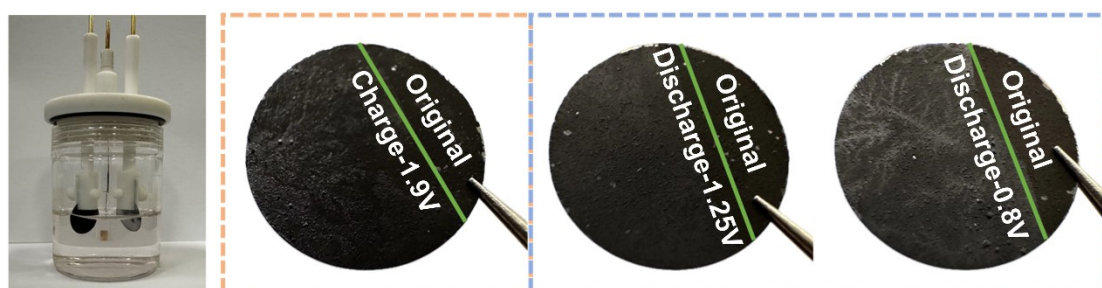
Figure S10. (a) Digital photos of the Zn//a-MnO$_2$/Ti$_3$C$_2$F three-electrode system and (b) a-MnO$_2$/Ti$_3$C$_2$F cathode at different potentials during charging and discharging.
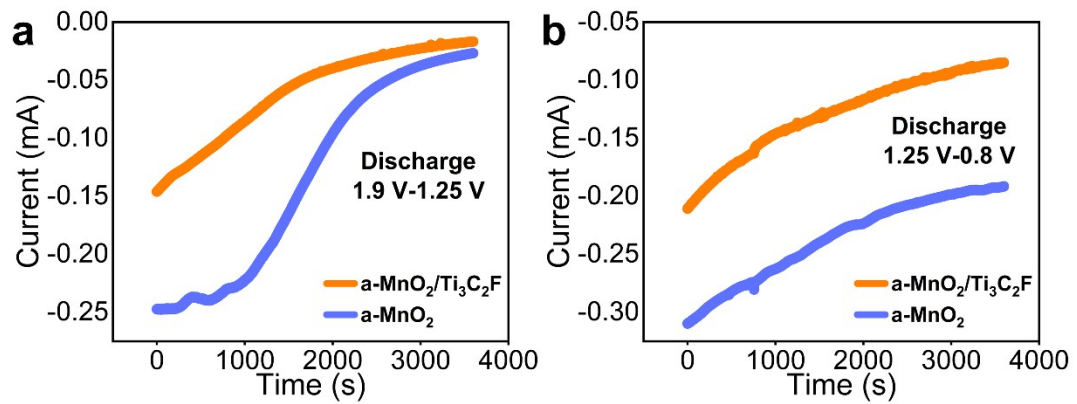
Figure S11. I-t curves of a-MnO$_2$/Ti$_3$C$_2$F and a-MnO$_2$ from 1.9 V to 1.25 V and then to 0.8 V discharges.
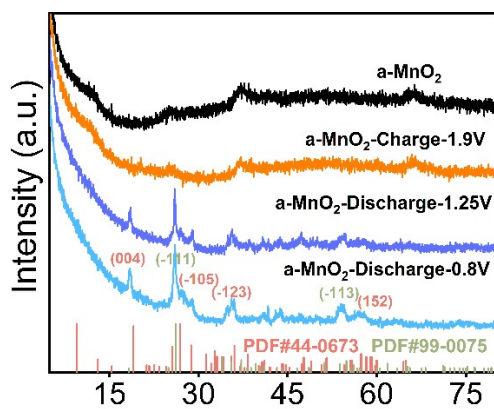
Figure S12. XRD patterns of a-MnO$_2$ cathode at different potentials during charging and discharging.

	wt%
C	24.11
O	22.27
F	2.88
S	4.94
Ti	0.81
Mn	23.07
Zn	21.91
Total:	100.00

	wt%
C	33.25
O	19.05
F	3.49
S	7.61
K	1.33
Ti	17.68
Mn	11.49
Zn	6.08
Total:	100.00
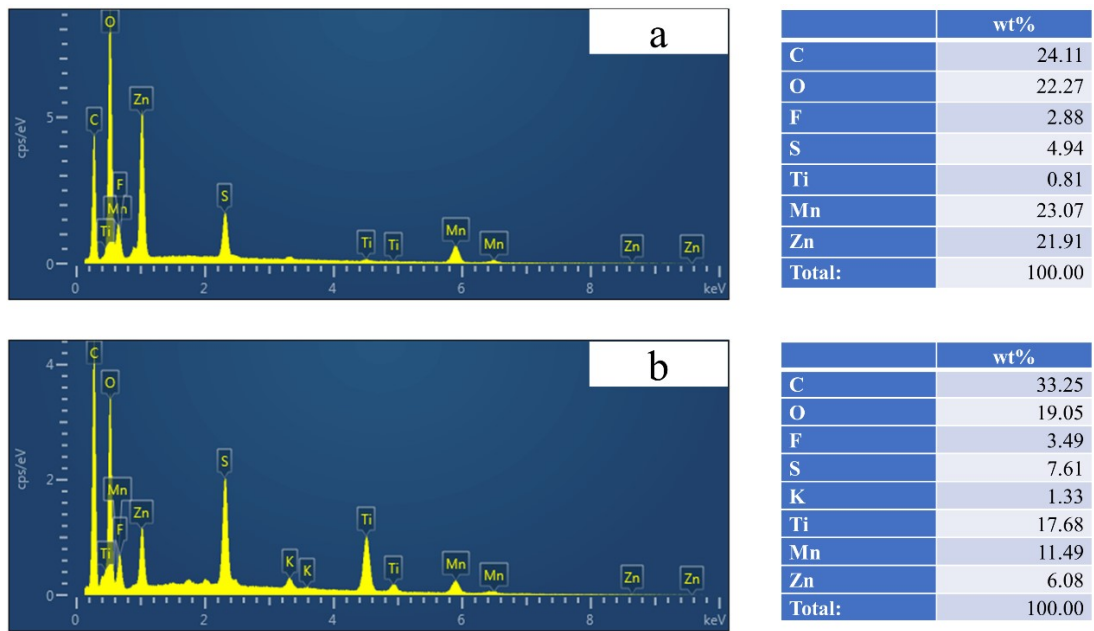
Figure S13. SEM-EDS element analysis of the (a) a-MnO$_2$ and (b) a-MnO$_2$/Ti$_3$C$_2$F electrodes at different charge-discharge states charged to 1.9 V and then charged to 1.25 V.

S4 Evaluation of electrode materials stabilities

Figure S14. Photographs of a-MnO$_2$/Ti$_3$C$_2$F and a-MnO$_2$ cathodes after 500 cycles under a current density of 0.3 A g^{-1}.
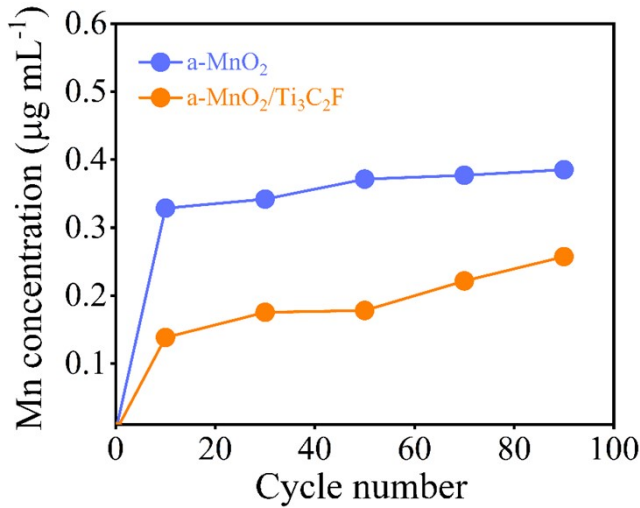
Figure S15. ICP analysis of dissolved Mn in electrolyte after various cycles for a-MnO$_2$/Ti$_3$C$_2$F and a-MnO$_2$ cathodes.

The International Conference on Thermal Analysis and Calorimetry indicates that a reliable thermodynamic model should be based on data obtained under multiple β values. In addition, the equal conversion method should be used to calculate the reaction kinetics. Therefore, in order to study the thermal stability of cathode materials, based on thermodynamic data obtained from DSC, we used Ozawa, Vyazovkin, and KAS models to calculate E_a at different heating rates s (β = 1, 2, 4, 7, and 10 ∘C/min). Thus, mutual authentication was achieved based on the accuracy of E_a values.[5]

The thermokinetic parameters of the Ozawa model are calculated using Eq. (1):

$$\ln \beta = \ln\left[\frac{AE_a}{RG(\alpha)}\right] - 2.315 - 0.4567\frac{E_a}{RT}$$

where α is the conversion degree of thermal reaction of electrode materials in batteries, A is the pre-exponential factor, T is the reaction temperature (K), R is the ideal gas constant (R = 8.314 J/(mol·K)), and $G(\alpha)$ is the conversion degree integral function. When α is fixed, $G(\alpha)$ is also fixed.

The thermokinetic parameters of the Vyazovkin model are calculated using Eq. (2):

$$-\ln t_{\alpha,t} = \ln\left[\frac{A}{G(\alpha)}\right] - \frac{E_a}{RT}$$

where $t_{\alpha, t}$ represents the time required for the electrode material to achieve different thermal conversion rates. The thermokinetic parameters of the KAS model are calculated by Eq. (3):

$$\ln\left(\frac{\beta}{T^2}\right) = \ln\left[\frac{AR}{E_a G(\alpha)}\right] - \frac{E_a}{RT}$$

In order to set a baseline when analyzing the data, we randomly selected 12 conversion degrees (α= 0.05, 0.1, 0.2, 0.3, 0.4, 0.5, 0.6, 0.7, 0.8, 0.9, 0.95, and 0.99) are used for thermodynamic analysis.[6]
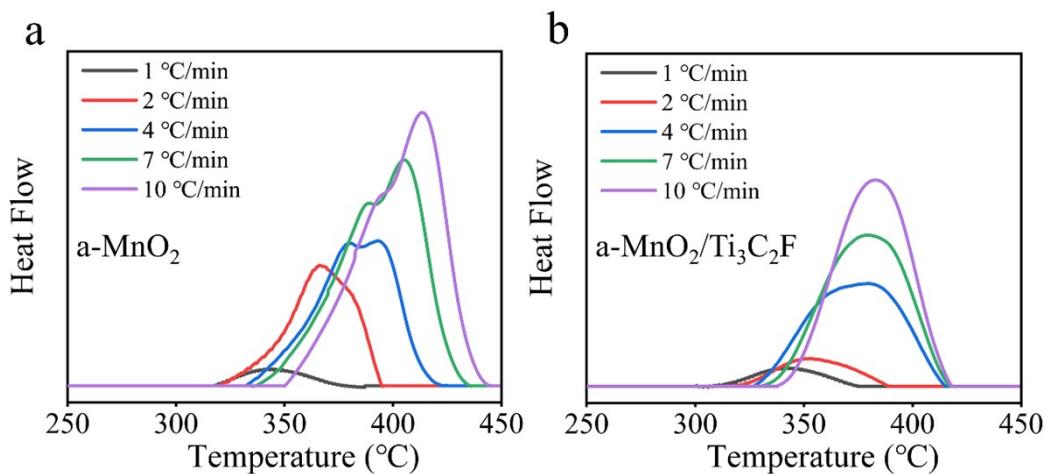
Figure S16. Heat absorption curves of a-MnO$_2$ and a-MnO$_2$/Ti$_3$C$_2$F at different heating rates.

S5 Density functional theory calculations

Our density functional theory (DFT) calculations[7, 8] were conducted using Vienna *ab initio* simulation package (VASP), employing plane-wave basis sets with the projector augmented-wave method.[9, 10] The exchange-correlation potential was treated using a generalized gradient approximation (GGA) with the Perdew-Burke-Ernzerhof (PBE) parametrization.[11] Additionally, we incorporated the van der Waals correction of Grimme's DFT-D3 model.[12] The energy cutoff was set to 520 eV, and the Brillouin-zone integration was sampled with a Γ-centered Monkhorst-Pack mesh of $2 \times 2 \times 1$.[13] Structural relaxations were performed until the maximum force on each atom was less than 0.01 eV/Å, and the energy convergence standard was 10^{-5} eV. Our calculations

utilized density functional theory with an applied Hubbard U (DFT+U) on the Mn (3.9 eV) d-orbitals, allowing for magnetic order with spin polarized calculations.[14] To determine the minimum-energy path and diffusion energy barrier of Zn diffusion along the interfaces, we employed the climbing-image nudged elastic band (CI-NEB) approach.
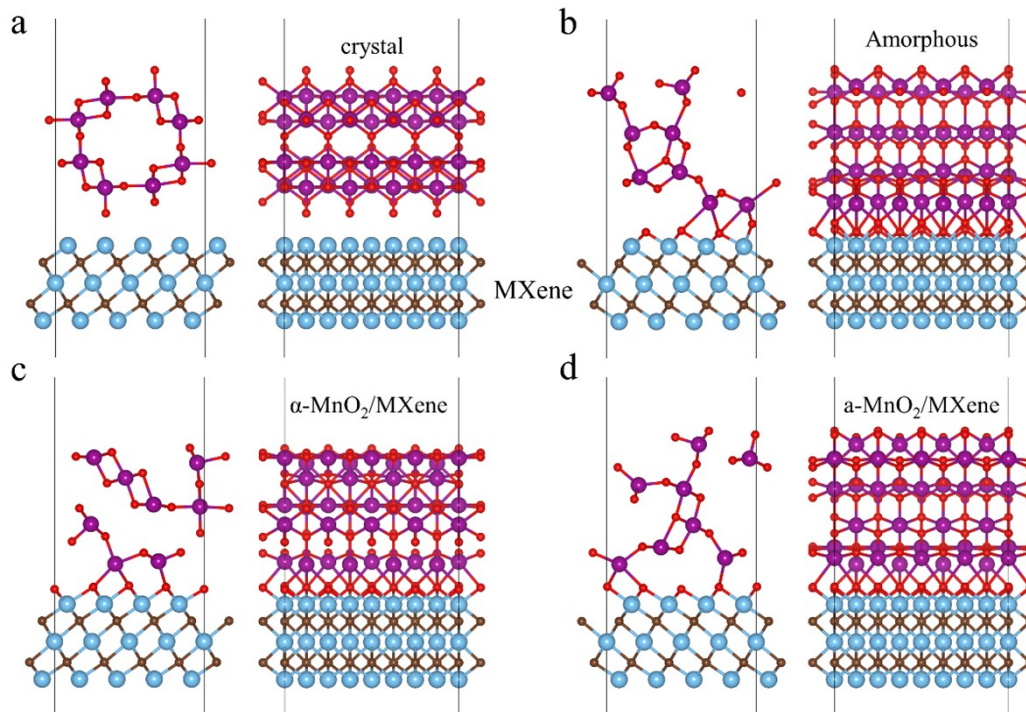
Figure S17. The calculation models of the (a-b) α-MnO_2, a-MnO_2 and MXene, as well as optimized (c-d) α-MnO_2/MXene and a-MnO_2/MXene structures.

Table S1 Rate performance of MnO_2 analogue materials reported in literatures.

Phase information	Rate performance	References
β-MnO_2	**205 mAh g^{-1} at 200** mA g^{-1}	**[15] J. Energy Chem. 56 (2021) 365–37**
β-MnO_2	193 mAh g^{-1} at 312 mA g^{-1}	**[16] Nano Energy 64 (2019) 103942**
α-MnO_2	96.8 mAh g^{-1} at 100 mA g^{-1}	**[17] Mater. Today Energy 16 (2020) 1003962**
layered-type MnO_2	146 mAh g^{-1} at 250 mA g^{-1}	**[18] Electrochim. Acta 276 (2018) 1-11**
α-MnO_2	260 mAh g^{-1} at 308 mA g^{-1}	**[19] Nat. Energy 1 (2016) 16039**
γ-MnO_2	<195 mAh g^{-1} at 100 mA g^{-1}	**[20] Nano-Micro Lett. 16 (2024) 109**
MON-coated MnO_2	209 mAh g^{-1} at 200 mAg^{-1}	**[21] ACS Nano 17 (2023) 5600−560**
β-MnO_2@C hybrids	< 120 mAh g^{-1} at 300 mAg^{-1}	**[22] J. Alloy. Compd.** 827 (2020) 154273
β-MnO_2@SWCNT	~235 mAh g^{-1} at 300 mAg^{-1}	**[23] Adv. Mater. 34 (2022) 2109872**
γ-MnO_2/MXene	287.3 mAh g^{-1} at 200 mAg^{-1}	**[24] J. Mater. Chem. A, 2020, 8, 24635–24644**
amorphous-MnO_2/Ti_3C_2F	384 mAh g^{-1} at 300 mAg^{-1}	**This work**

Table S2. a-MnO$_2$/Ti$_3$C$_2$F's GITT corresponding data.

	a-MnO$_2$/Ti$_3$C$_2$F		
Record (min)	Potential (V)	D (cm^2/s)	logD
92	1.5258	8.11661×10^{-5}	-4.090625169
153.5	1.6157	5.29600×10^{-5}	-4.276051981
214.5	1.6735	1.94329×10^{-5}	-4.711460858
275.5	1.5095	8.16773×10^{-5}	-4.087898806
322.5	1.4716	1.61107×10^{-4}	-3.792885179
383.5	1.3915	9.77024×10^{-5}	-4.01009499
444.5	1.3467	5.73523×10^{-6}	-5.241449137
505.5	1.3608	1.37014×10^{-6}	-5.863235243
566.5	1.3572	4.17483×10^{-6}	-5.379360742
627.5	1.3524	5.82346×10^{-6}	-5.234818705
688.5	1.3488	1.92905×10^{-6}	-5.714655421
749.5	1.3505	2.67286×10^{-4}	-3.573022985
Average		6.50304×10^{-5}	-4.664629935

Table S3. a-MnO$_2$'s GITT corresponding data.

	a-MnO$_2$		
Record (min)	Potential (V)	D (cm^2/s)	logD
92	1.5352	5.29701×10^{-5}	-4.275968955
153.5	1.6297	3.40659×10^{-5}	-4.46767978
214.5	1.6707	4.19719×10^{-6}	-5.377040752
275.5	1.6875	1.55249×10^{-7}	-6.808969925
322.5	1.6876	2.41489×10^{-4}	-3.617102146
383.5	1.5287	1.25656×10^{-4}	-3.900815628
444.5	1.4333	9.61150×10^{-5}	-4.017208673
505.5	1.3524	3.02991×10^{-6}	-5.518570978
566.5	1.3622	2.19753×10^{-8}	-7.658064215
627.5	1.3430	2.56029×10^{-6}	-5.591709162
688.5	1.3574	2.33078×10^{-6}	-5.632499291
749.5	1.3381	2.46099×10^{-6}	-5.608888415
810.5	1.3507	1.54199×10^{-5}	-4.811915636
871.5	1.3475	6.81411×10^{-5}	-4.166591068
Average		4.63295×10^{-5}	-5.103787473

Table S4. E_a and R^2 values calculation for the cathode material of a-MnO_2/Ti_3C_2F using three models under different α values.

α	Ozawa		Vyazovkin		KAS	
	E_a (kJ/mol)	R^2	E_a (kJ/mol)	R^2	E_a (kJ/mol)	R^2
5	187.736	0.998	160.552	0.977	187.493	0.997
10	185.436	0.993	158.062	0.966	185.001	0.993
20	181.716	0.988	154.112	0.953	180.984	0.987
30	177.013	0.982	149.366	0.939	175.960	0.980
40	174.067	0.972	146.152	0.921	172.789	0.969
50	169.259	0.960	141.314	0.900	167.669	0.955
60	167.486	0.952	139.504	0.889	165.737	0.947
70	166.492	0.940	138.208	0.870	164.619	0.933
80	164.586	0.927	136.243	0.852	162.539	0.918
90	164.215	0.918	135.807	0.841	162.053	0.908
95	163.663	0.909	135.068	0.828	161.400	0.898
99	162.362	0.912	133.924	0.831	159.934	0.901
Average	172.002	0.954	144.026	0.897	170.514	0.948

Table S5. E_a and R^2 values calculation for the cathode material of a-MnO$_2$ using three models under different α values.

α	Ozawa E_a (kJ/mol)	R^2	Vyazovkin E_a (kJ/mol)	R^2	KAS E_a (kJ/mol)	R^2
5	160.048	0.997	136.091	0.990	158.224	0.996
10	150.532	0.995	127.321	0.988	148.133	0.995
20	140.219	0.988	117.810	0.979	137.178	0.987
30	135.191	0.989	113.004	0.976	131.801	0.987
40	129.872	0.990	108.112	0.977	126.128	0.988
50	126.754	0.992	105.235	0.979	122.777	0.990
60	125.754	0.992	104.119	0.975	121.656	0.991
70	125.999	0.992	104.251	0.973	121.847	0.991
80	128.362	0.992	106.391	0.973	124.259	0.991
90	130.349	0.993	108.177	0.973	126.259	0.992
95	131.499	0.996	109.117	0.973	127.391	0.995
99	144.943	0.988	120.847	0.953	141.363	0.986
Average	135.793	0.992	113.372	0.975	132.251	0.990

REFERENCES

1. Huang, J.; Tang, X.; Liu, K.; Fang, G.; He, Z.; Li, Z., Interfacial chemical binding and improved kinetics assisting stable aqueous Zn-MnO$_2$ batteries. Materials Today Energy **2020,** 17.

2. Li, X.; Ji, C.; Shen, J.; Feng, J.; Mi, H.; Xu, Y.; Guo, F.; Yan, X., Amorphous Heterostructure Derived from Divalent Manganese Borate for Ultrastable and Ultrafast Aqueous Zinc Ion Storage. Adv. Sci. **2023,** 10.

3. Liu, W.; Su, Q.; Zhu, R.; Shi, W.; Zhang, F.; Du, G.; Zhao, W.; Zhang, M.; Xu, B., Chemical Lithiation-Induced Oxygen Vacancies in MnO$_2$ at Room Temperature for Aqueous Zinc-Ion Batteries. ACS Appl. Energy Mater. **2023,** 6.

4. Chen, Q.; Lou, X.; Yuan, Y.; You, K.; Li, C.; Jiang, C.; Zeng, Y.; Zhou, S.; Zhang, J.; Hou, G.; Lu, J.; Tang, Y., Surface Adsorption and Proton Chemistry of Ultra-Stabilized Aqueous Zinc–Manganese Dioxide Batteries. Adv. Mater. **2023,** 35.

5. Zhang, C.-Z.; Jiang, J.-C.; Huang, A.-C.; Tang, Y.; Xie, L.-J.; Zhai, J.; Xing, Z.-X., A novel multifunctional additive strategy improves the cycling stability and thermal stability of SiO/C anode Li-ion batteries. Process Saf. and Environ. Protect. **2022,** 164.

6. Wu, Z.-H.; Wu, Y.; Tang, Y.; Jiang, J.-C.; Huang, A.-C., Evaluation of composite flame-retardant electrolyte additives improvement on the safety performance of lithium-ion batteries. Process Saf. and Environ. Protect. **2023,** 169.

7. Hohenberg, P.; Kohn, W., Inhomogeneous Electron Gas. Phys. Rev. B **1964,** 136.

8. Kohn, W.; Sham, L. J., Self-Consistent Equations Including Exchange and Correlation Effects. Physical Review **1965,** 140.

9. Blöchl, P. E., Projector augmented-wave method. Phys. Rev. B **1994,** 50.

10. Kresse, G.; Furthmuller, J. Efficient iterative schemes for ab initio total-energy calculations using a plane-wave basis set. Phys. Rev. B **1996**, 54.

11. John P. P.; Kieron, B. Matthias Ernzerhof. Generalized Gradient Approximation Made Simple. Phys. Rev. Lett. **1996**, 77.

12. Grimme, S.; Antony, J.; Ehrlich, S.; Krieg, H., A consistent and accurate ab initio parametrization of density functional dispersion correction (DFT-D) for the 94 elements H-Pu. J. Chem. Phys. **2010,** 132.

13. Monkhorst, H. J.; Pack, J. D., Special points for Brillouin-zone integrations. Phys. Rev. B **1976,** 13.

14. Dudarev, S.L.; Botton, G.A.; Savrasov, S.Y.; Humphreys, C.J. Electron-energy-loss spectra and the structural stability of nickel oxide: An LSDA1U study. Phys. Rev. Lett. **1998**, 57.

15. Liu, W.; Zhang, X.; Huang, Y.; Jiang, B.; Chang, Z.; Xu, C.; Kang, F., β-MnO$_2$ with proton conversion mechanism in rechargeable zinc ion battery. J. Energy Chem. **2021,** 56.

16. Liu, M.; Zhao, Q.; Liu, H.; Yang, J.; Chen, X.; Yang, L.; Cui, Y.; Huang, W.; Zhao, W.; Song, A.; Wang, Y.; Ding, S.; Song, Y.; Qian, G.; Chen, H.; Pan, F., Tuning phase evolution of β-MnO$_2$ during microwave hydrothermal synthesis for high-performance aqueous Zn ion battery. Nano Energy **2019,** 64.

17. Guo, X.; Zhou, J.; Bai, C.; Li, X.; Fang, G.; Liang, S., Zn/MnO$_2$ battery chemistry with dissolution-deposition mechanism. Mater. Today Energy **2020,** 16.

18. Muhammad H. A.; Saiful I.; Dimas Y. P.; Vinod M.; Sungjin K.; Jeonggeun J.; Seokhun K.; Yang-Kook S.; Kwangho K.; Jaekook K., Structural transformation and electrochemical study of layered MnO_2 in rechargeable aqueous zinc-ion battery, Electrochim. Acta **2018,** 276.

19. Pan, H.; Shao, Y.; Yan, P.; Cheng, Y.; Han, K. S.; Nie, Z.; Wang, C.; Yang, J.; Li, X.; Bhattacharya, P.; et al., Reversible aqueous zinc/manganese oxide energy storage from conversion reactions, Nature Energy **2016,** 1.

20. Lv, W.; Shen, Z.; Li, X.; Meng, J.; Yang, W.; Ding, F.; Ju, X.; Ye, F.; Li, Y.; Lyu, X.; et al., Discovering Cathodic Biocompatibility for Aqueous Zn–MnO_2 Battery: An Integrating Biomass Carbon Strategy, Nano-Micro Lett. **2024,** 16.

21. Zuo, Y.; Meng, T.; Tian, H.; Ling, L.; Zhang, H.; Zhang, H.; Sun, X.; Cai, S., Enhanced H^+ Storage of a MnO_2 Cathode via a MnO_2 Nanolayer Interphase Transformed from Manganese Phosphate, ACS Nano **2023,** 17.

22. Jiang, W.; Xu, X.; Liu, Y.; Tan, L.; Zhou, F.; Xu, Z.; Hu, R., Facile plasma treated β-MnO_2@C hybrids for durable cycling cathodes in aqueous Zn-ion batteries, J. Alloys Compd. **2020,** 827.

23. He, P.; Huang, J., Chemical Passivation Stabilizes Zn Anode, Adv. Mater. **2022,** 34.

24. Shi, M.; Wang, B.; Chen, C.; Lang, J.; Yan, C.; Yan, X., 3D high-density MXene@MnO_2 microflowers for advanced aqueous zinc-ion batteries, J. Mater. Chem. A **2020,** 8.